



# DEM modeling of hydraulic fracturing in permeable rock: influence of viscosity, injection rate and in situ states

Kang Duan<sup>1,2</sup> · Chung Yee Kwok<sup>2</sup> · Wei Wu<sup>1</sup> · Lu Jing<sup>2</sup>

Received: 16 May 2017 / Accepted: 9 January 2018 / Published online: 21 February 2018  
© Springer-Verlag GmbH Germany, part of Springer Nature 2018

## Abstract

Hydraulic fracturing in permeable rock is a complicated process which might be influenced by various factors including the operational parameters (e.g., fluid viscosity, injection rate and borehole diameter) and the in situ conditions (e.g., in situ stress states and initial pore pressure level). To elucidate the effects of these variables, simulations are performed on hollow-squared samples at laboratory scale using fully coupled discrete element method. The model is first validated by comparing the stress around the borehole wall measured numerically with that calculated theoretically. Systematic parametric studies are then conducted. Modeling results reveal that the breakdown pressure and time to fracture stay constant when the viscosity is lower than 0.002 Pa s or higher than 0.2 Pa s but increases significantly when it is between 0.002 and 0.2 Pa s. Raising the injection rate can shorten the time to fracture but dramatically increase the breakdown pressure. Larger borehole diameter leads to the increase in the time to fracture and the reduction in the breakdown pressure. Higher in situ stress requires a longer injection time and higher breakdown pressure. The initial pore pressure, on the other hand, reduces the breakdown pressure as well as the time to fracture. The increase in breakdown pressure with viscosity or injection rate can be attributed to the size effect of greater tensile strength of samples with smaller infiltrated regions.

**Keywords** Discrete element method · Fluid viscosity · Hydraulic fracturing · Injection rate · In situ conditions

## 1 Introduction

Hydraulic fracturing has been widely used in the energy industry, e.g., the stimulation of unconventional gas/oil reservoirs, the enhancement of geothermal system and the determination of in situ stress states [7, 27, 31, 37]. Initiation and propagation of injection-induced fractures might be extremely complicated due to the heterogeneous characteristic of rock properties as well as the sophisticated in situ conditions and operational parameters. Many factors, including the in situ stress states, the pore pressure level, the injection fluid viscosity and injection rate, might

affect the initiation, propagation and ultimate patterns of hydraulic fractures [3, 32, 38]. Full understanding of the influence of these factors is essential for engineers to be able to control the fracture geometry, to optimize the operational parameters and to maximize the engineering benefits.

Plenty of experimental studies have been performed in the laboratory to investigate the hydraulic fracturing in cylindrical/cubic specimens with or without the application of confining pressures. Different types of rocks have been tested, including shale, coal, granite, sandstone and artificial materials [13, 36]. Experimental results indicated that rock texture like grain size considerably affects the geometry of hydraulically induced fractures. Effects of other factors, e.g., the existing of fractures [38], borehole diameter [18], the variation of confining pressure [3] and the various injection fluids [34], have been examined. Although comparative tests have been designed to evaluate the effect of different factors, it was relatively hard to isolate the influence of a single factor in the laboratory due to the heterogeneity lies in rock properties.

✉ Chung Yee Kwok  
fkwok8@hku.hk

✉ Wei Wu  
wu.wei@ntu.edu.sg

<sup>1</sup> School of Civil and Environmental Engineering, Nanyang Technological University, Singapore, Singapore

<sup>2</sup> Department of Civil Engineering, The University of Hong Kong, Hong Kong, Hong Kong

Numerous attempts have been made to forecast the magnitude of breakdown pressure by analytical, semi-analytical and numerical approaches [1, 12, 17, 23, 24]. The theory of effective stress suggests that the breakdown pressure of a borehole should be a function of ambient stress and strength of the rock alone. However, in the laboratory hydraulic fracturing tests on borehole with finite length, it was found that the breakdown pressure is a strong function of fracturing fluid composition and state as well [12, 34, 38]. Moreover, the possible dependency of the fracturing behavior of rock material upon the rate of borehole pressurization, fluid rheology and fluid additives has been recognized but not thoroughly elucidated [3].

The numerical approaches adopted to simulate hydraulic fracturing can be generally classified into the continuum and discontinuous categories [6, 14, 33]. Most of the continuous methods are based on several assumptions and simplifications such as isotropic and homogeneous material, linear elastic deformation and assumption of linear elastic fracture mechanics for fracture growth [1]. Discrete element method (DEM), on the other hand, can explicitly represent grain-scale microstructural features of rock, and thus provides a robust tool to examine the mechanics of fracture propagation during hydraulic fracturing [2]. A number of studies have been conducted using the flow-coupled DEM models to simulate the hydraulic fractures in either intact or fractured rock formations [2, 11, 28, 35]. Most recently, the hydro-thermo-mechanical coupled modeling of hydraulic fracturing has also been conducted [29, 30]. In fact, most of these applications focused on the fracture process, ultimate patterns or the interaction between induced and preexisting fractures. Rare attention has been paid to the quantitative response, especially the variation of breakdown pressure versus operational parameters and in situ states. A well-designed DEM model can provide quantitative estimation of the response during hydraulic fracturing, provided that the model is strictly validated and the boundary conditions are rigorously controlled.

In the current study, a series of parametric studies are performed at laboratory scale to evaluate the dependency of hydraulic fracturing on various factors including the fluid viscosity, injection rate, in situ stress states, the borehole diameter and the initial pore pressure. Particular attentions are focused on the breakdown pressure and the time to fracture. Comparison between the poroelasticity theory and the simulation results is also carried out to elucidate the mechanisms contributing to the discrepancies between the theoretical and numerical results.

## 2 Numerical methodology

In the DEM model, the rock matrix is represented as an assembly of separate particles, which are bonded at their contacts (the bonded-particle model) [5, 26]. Movement of the particles is described by the Newton's second law, while the interaction forces between them are dominated by the force–displacement law, for which the linear contact model is used in this study. Bonds between particles may break once the stress acting on them exceeds the corresponding strength. In our study, the bond breakage is regarded as a tensile crack if its failure is caused by tensile stress; otherwise, it is defined as a shear crack [9]. The bonded-particle model has been extensively applied in the simulation of mechanical responses of rock under various stress conditions with great success [4, 19, 22, 25]. In the modeling of hydraulic fracturing, a popular method is to couple DEM with a fluid flow algorithm that considers the hydromechanics of interstitial fluids, which is briefly introduced as follows.

The fluid flow algorithm in the DEM model is implemented based on the assumption of individual reservoirs and pipe network [21]. As illustrated in Fig. 1, a series of enclosed domains (also known as reservoirs, represented as blue dots) are created by connecting the centers of adjunct particles [28]. Adjacent reservoirs are connected by particle contact which can also serve as fluid flow path. The reservoirs may have certain volume and can also store some fluid pressure. Thus, fluid flow occurs through the pipes once pressure difference exists between the reservoirs at the two ends. The rate of fluid flow can be described by [2]:

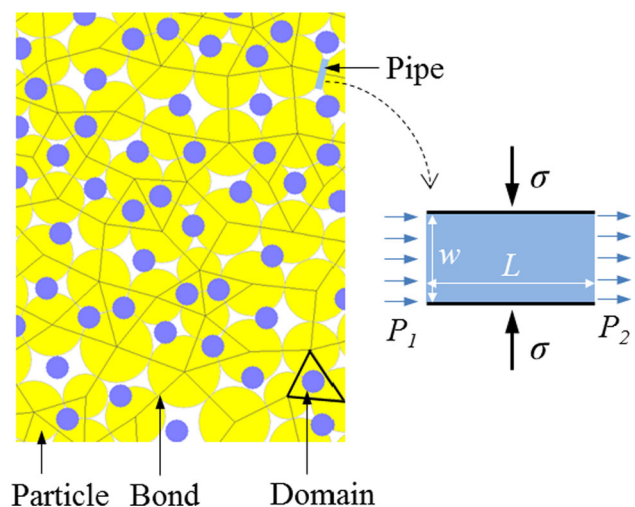


**Fig. 1** Schematic diagram illustrates the reservoirs (blue dots), flow paths (contacts between particles), and bonds (black lines) in compact bonded assembly of particles (yellow disks) (after Itasca 2008) (color figure online)

$$Q = \frac{w^3}{12\mu} \frac{P_1 - P_2}{L} \quad (1)$$

where  $w$  is the aperture of the pipe,  $P_1$  and  $P_2$  represent the pressure in the two reservoirs across the pipe,  $L$  is the length of the pipe, and  $\mu$  is the viscosity of the fluid.

In one time step ( $\Delta t$ ), the flow from surrounding pipes leads to the change of volume in each reservoir ( $\sum Q\Delta t$ ), which ultimately results in the increase in fluid pressure ( $\Delta P$ ) in the reservoir by [2]:

$$\Delta P = \frac{K_f}{V_d} \left( \sum Q\Delta t - \Delta V_d \right) \quad (2)$$

where  $K_f$  is the fluid bulk modulus,  $V_d$  is the volume of the reservoir, and  $\Delta V_d$  is the mechanical change in volume of the reservoir.

The normal stress acting on the pipe ( $\sigma$ ) could affect its aperture by [5, 21]:

$$w = \frac{w_0\sigma_0}{\sigma + \sigma_0} \quad (3)$$

where  $\sigma_0$  is the normal stress at which the pipe aperture reduces to half of its residual aperture ( $w_0$ ).

Fully hydromechanical coupling exists between the rock matrix and the fluid as fluid flow is simulated at the particle scale. Therefore, increasing in connectivity between reservoirs is automatically considered as increase in aperture and the formation of new cracks. In this manner, it is possible to simulate evolution of fracture volume change and network connectivity, as a result of fluid injection.

### 3 Setup and validation of the numerical model

#### 3.1 Setup of the DEM model

The DEM model used to simulate the hydraulic fracturing is presented in Fig. 2a. A hollow-squared sample is generated with the scale of 50 mm  $\times$  50 mm. A borehole for the injection of fluid is created at the center of the model. The diameter of the borehole ( $D$ ) equals to 10 mm. The particle size follows the uniform distribution with  $R_{\min} = 0.2$  mm and  $R_{\max}/R_{\min} = 1.66$ . There are altogether 10,015 particles in the model with about 20 particles cross the borehole diameter. Microparameters used in the DEM model originate from those calibrated to represent the matrix of Mancos shale in our previous studies on borehole breakout (Duan et al. 2016). The corresponding values can be found in Table 1. At the macroscale, the uniaxial compressive strength equals to 77.8 MPa, the Young's modulus equals to 28.8 GPa, the Poisson's ratio is 0.27, and the direct tensile strength equals to 15.3 MPa. It

is important to mention that these properties are obtained from the uniaxial compressive test and direct tensile test conducted on samples with size of 50  $\times$  25 mm. Previous studies have confirmed the scale effect on tensile strength of DEM model [26]. The relationship between this effect and the hydraulic fracturing will be discussed in Sect. 5.

Before the conduction of fluid injection, in situ stresses and initial pore pressure are first applied to the designed level. After that, fluid injection is implemented on the saturated sample through the reservoir in the center (see the pipe network illustrated in Fig. 2a) with constant injection rate until the borehole is pressurized to failure. During the fluid injection process, the in situ stresses are maintained constant by adjusting the positions of corresponding walls through servomechanism. Initial input parameters used to define the fluid flow properties are listed in Table 2. Instead of reproducing the hydraulic fracturing tests conducted on a specific rock type, we are more interested in performing a general study with the aim of investigating the influences of various factors on the hydraulic fracturing in permeable rock formation.

#### 3.2 Validation of the DEM model

In the linear elastic and isotropic rock formation, stress distribution around the opening can be calculated by assuming that the pore pressure in the formation is constant and the borehole fluid does not communicate with the pore fluid in the rock, and that [16, 37]:

$$\sigma_{rr} = \frac{\sigma_H + \sigma_h}{2} \left( 1 - \frac{a^2}{r^2} \right) + \frac{\sigma_H - \sigma_h}{2} \left( 1 - 4 \frac{a^2}{r^2} + 3 \frac{a^4}{r^4} \right) \cos 2\theta + \Delta P \frac{a^2}{r^2} \quad (4.a)$$

$$\sigma_{\theta\theta} = \frac{\sigma_H + \sigma_h}{2} \left( 1 + \frac{a^2}{r^2} \right) - \frac{\sigma_H - \sigma_h}{2} \left( 1 + 3 \frac{a^4}{r^4} \right) \cos 2\theta - \Delta P \frac{a^2}{r^2} \quad (4.b)$$

$$\sigma_z = \sigma_v - 2\nu(\sigma_H - \sigma_h) \cos 2\theta \quad (4.c)$$

$$\sigma_{r\theta} = \frac{\sigma_H - \sigma_h}{2} \left( 1 + 2 \frac{a^2}{r^2} - 3 \frac{a^4}{r^4} \right) \sin 2\theta \quad (4.d)$$

where  $\sigma_{rr}$ ,  $\sigma_{\theta\theta}$ ,  $\sigma_z$  and  $\sigma_{r\theta}$  represent the radial, tangential, vertical and shear stresses around the hole wall, respectively.  $\sigma_H$  and  $\sigma_h$  are the maximum and minimum far-field stresses.  $\sigma_v$  is the vertical in situ stress, which is assumed to be zero for the 2D model.  $a$  is the hole radius, and  $r$  is the distance from the point of interest to the hole center (see Fig. 2b).  $\theta$  is the angle measured counterclockwise from the direction of maximum in situ stress.  $\Delta P$  equals to the difference between fluid pressure inside the hole ( $P_w$ ) and the pore pressure in the formation ( $P_0$ ).

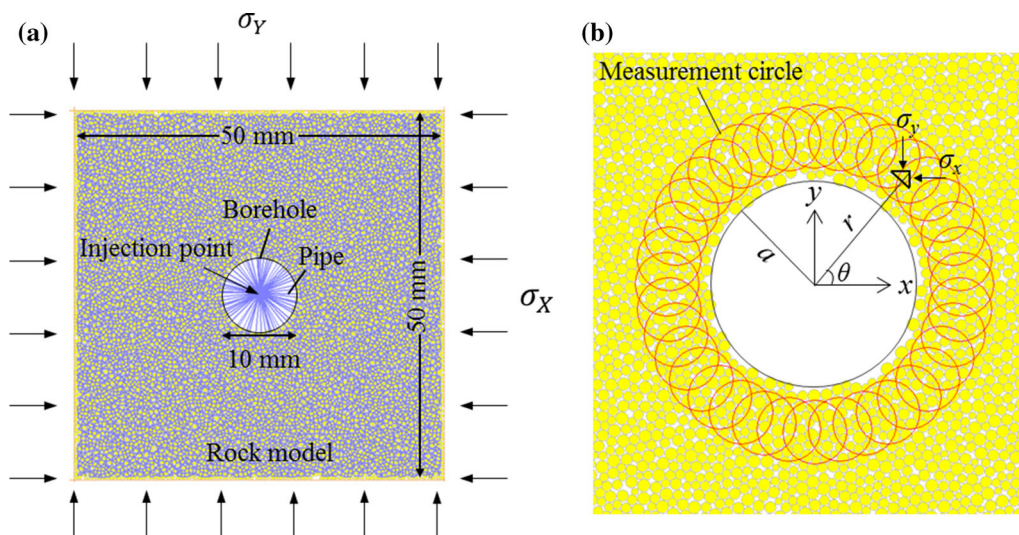


**Fig. 2** **a** Setup of the hollow-squared DEM model for the simulation of hydraulic fracturing. Fluid injection is implemented through the reservoir in the center of the borehole. Blue lines represent the fluid flow network. **b** Distribution of the measurement circles around the borehole. Twenty-four measurement circles with angular distance of 15° are installed. The diameter of the measurement circles equals to 3 mm. The distance between the centers of measurement circles and the borehole center is 7 mm (color figure online)

**Table 1** Microparameters used in the DEM model

Particle properties	Value	Bond properties	Value
The contact modulus, $E_c$ (GPa)	23	The parallel bond modulus, $\bar{E}_c$ (GPa)	23
Ratio between normal and shear stiffness of particles, $k_n/k_s$	2.5	Ratio between normal and shear stiffness of parallel bond, $\bar{k}^n/\bar{k}^s$	2.5
Coefficient of friction $\bar{\mu}$	0.5	Tensile strength of parallel bond, $\bar{\sigma}_c$ (MPa)	60 ± 13.5
The particle radius ratio, $R_{max}/R_{min}$	1.66	Shear strength of parallel bond, $\bar{\tau}_c$ (MPa)	60 ± 13.5
The minimum particle radius, $R_{min}$ (mm)	0.2	The parallel bond radius ratio, $\bar{\lambda}$	1.0
Density, $\rho$ (kg/m <sup>3</sup> )	3169		

These parameters were initially calibrated to represent the rock matrix of Mancos shale in the study of Ref. [10]

**Table 2** Microparameters used for the fluid flow coupling model

Parameters	Value
Initial aperture, $w_0$ (m)	$1 \times 10^{-6}$
Bulk modulus of the injection fluid, $K_f$ (GPa)	2
Pressure when the aperture decreases to half, $P_0$ (MPa)	20
Fluid injection rate (m <sup>3</sup> /s)	$2.12 \times 10^{-12}$
Fluid viscosity, $\mu$ (Pa s)	0.2

The operational parameters including the fluid viscosity and the injection rate are varied to investigate their effects on the propagation of hydraulic fractures

In the DEM model, the stress state around the borehole wall can be estimated by measurement circles. As illustrated in Fig. 2b, 24 measurement circles are installed into the numerical model. Stresses measured by these circles

( $\sigma_x$ ,  $\sigma_y$  and  $\tau_{xy}$ ) can be transformed into the polar coordination following [8]:

$$\sigma_{rr} = \sigma_x \cos^2 \theta + \sigma_y \sin^2 \theta + 2\tau_{xy} \sin \theta \cos \theta \tag{5.a}$$

$$\sigma_{\theta\theta} = \sigma_x \sin^2 \theta + \sigma_y \cos^2 \theta - 2\tau_{xy} \sin \theta \cos \theta \tag{5.b}$$

$$\sigma_{r\theta} = (\sigma_y - \sigma_x) \sin \theta \cos \theta + \tau_{xy}(\cos^2 \theta - \sin^2 \theta) \tag{5.c}$$

To validate the numerical model, fluid injection is carried out with a relative low rate of  $2.12 \times 10^{-12}$  m<sup>3</sup>/s. The in situ stress state is  $\sigma_x = 15$  MPa,  $\sigma_y = 10$  MPa and the initial pore pressure  $P_0 = 1.0$  MPa. Three stages before the occurrence of bond breakage are considered, i.e., 8000, 20,000 and 40,000 steps after injection. The corresponding injection pressure ( $P_w$ ) equals to 15.25, 29.48 and 41.18 MPa, respectively.

Figure 3 compares the stress distributions around the borehole wall calculated from the analytical solutions with those measured from the DEM model. In this study,

compressive stresses are positive. Excellent agreement can be found between the analytical and numerical results, in terms of the magnitude and the fluctuation characteristic of three stress components. The radial stress ( $\sigma_{rr}$ ) stays almost constant with its magnitude increases from  $\sim 12$  to  $\sim 26$  MPa from stage (a) to stage (c). Periodic fluctuation can be noted from the tangential stress ( $\sigma_{\theta\theta}$ ) and the shear stress ( $\sigma_{r\theta}$ ). The maximum value of  $\sigma_{\theta\theta}$  is obtained when  $\theta = 90^\circ$  and  $270^\circ$ , which aligns with the orientation of minimum stress ( $\sigma_Y$ ). The magnitude of  $\sigma_{\theta\theta}$  reduces gradually with the ongoing of injection. The magnitude of  $\sigma_{\theta\theta}$  becomes negative at stage (b) (Fig. 3b), which indicates that the borehole wall turns to be under tension in the tangential orientation. The maximum tensile stress in the tangential orientation continually increases to  $\sim 10$  MPa at stage (c), and the injection-induced tensile fracture tends to be formed at these orientations (when  $\theta = 0^\circ$  and  $180^\circ$ ). The maximum value of  $\sigma_{r\theta}$  exists when  $\theta = 145^\circ$  and  $325^\circ$ . The magnitude of  $\sigma_{r\theta}$  is independent of the injection pressure. In general, the influence of both the in situ stress and the injection pressure can be captured by the DEM model. Therefore, it can be adopted to quantitatively assess the injection-induced fracture responses of rock with various operational and in situ conditions.

## 4 Simulation results

In this section, effects of various factors, which can be classified into the operational parameters (fluid viscosity, injection rate and borehole diameter) and the in situ conditions (in situ stress states, initial pore pressure), are systematically evaluated by examining the variation of breakdown pressure and time to fracture. Spatial distribution of cracks at the end of each test is plotted to indicate the geometry of hydraulic-induced fractures. Moreover, the mechanisms at particle scale can be recognized from the percentage of shear cracks as summarized in Table 3.

### 4.1 Propagation of the hydraulic fractures

One typical case demonstrating the process of hydraulic fracturing is presented in Fig. 4. The initial pore pressure  $P_0 = 1.0$  MPa, and the in situ stress state  $\sigma_X = 15$  MPa,  $\sigma_Y = 10$  MPa. As illustrated in Fig. 4a, the well pressure increases linearly at the initial stage with no microcracks occur until the injection is conducted after 2400 s. Once the well pressure reaches the critical value (the breakdown pressure), propagation of the induced tensile fracture occurs. This unstable fracture growth is accompanied by a

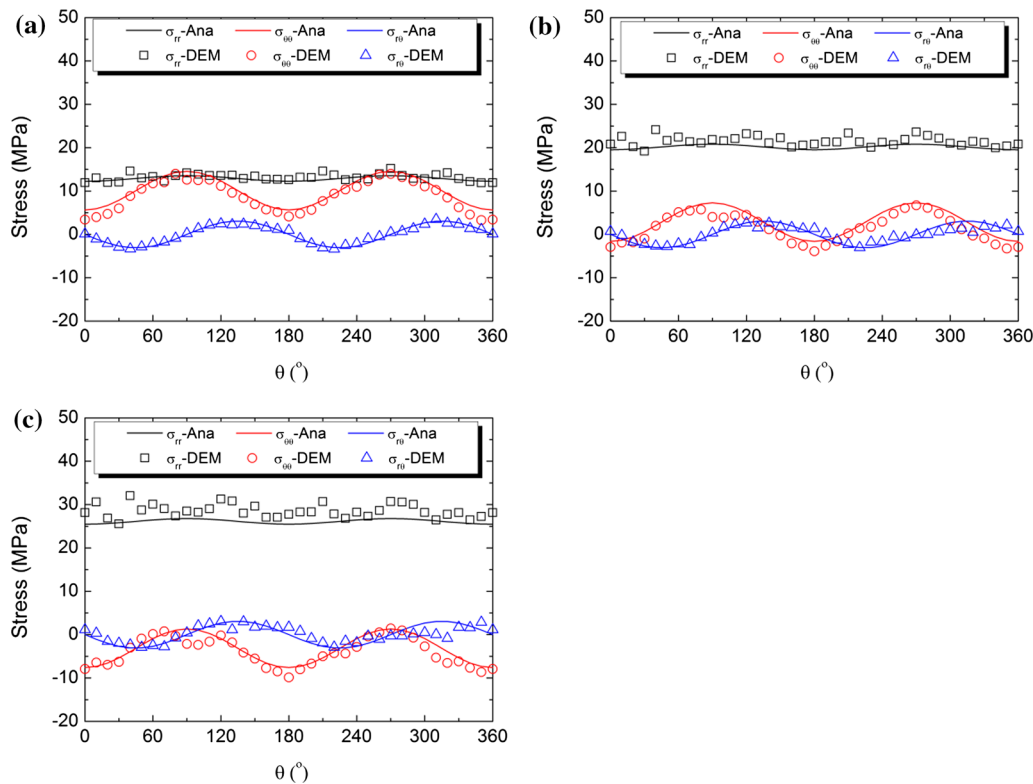


**Fig. 3** Comparison between the stresses measured from the DEM model (open dots) and those calculated from the analytical solutions (solid lines) when the fluid pressure is: **a** 15.25 MPa, **b** 29.48 MPa and **c** 41.18 MPa. The corresponding calculation steps equal to 8000 steps, 20,000 steps and 40,000 steps, respectively. The in situ stress state:  $\sigma_X = 15$  MPa,  $\sigma_Y = 10$  MPa. The initial pore pressure  $P_0 = 1.0$  MPa. The injection rate is  $2.12 \times 10^{-12}$  m<sup>3</sup>/s, and the fluid viscosity equals to 0.2 Pa s

**Table 3** Summary of the percentage of shear cracks at the end of hydraulic fracturing tests conducted on models with different operational parameters and in situ states

Fluid viscosity		Injection rate		Borehole diameter		In situ stress		Minimum principal stress		Initial pore pressure	
$\mu$ (Pa s)	Percentage of shear crack (%)	Injection rate (m <sup>3</sup> /s)	Percentage of shear crack (%)	D (mm)	Percentage of shear crack (%)	$\sigma_x = \sigma_y$ (MPa)	Percentage of shear crack (%)	$\sigma_x$ (MPa)	Percentage of shear crack (%)	$P_0$ (MPa)	Percentage of shear crack (%)
0.0002	3.2 (4/125)	$2.12 \times 10^{-12}$	0.8 (1/134)	4	1.6 (2/124)	0	1.7 (2/120)	8	0.0 (0/113)	1.0	2.3 (5/219)
0.002	1.7 (3/177)	$5.0 \times 10^{-12}$	0.8 (1/122)	6	1.8 (2/111)	5	1.4 (4/159)	16	0.0 (0/114)	5.0	0.5 (1/199)
0.02	2.3 (4/173)	$2.12 \times 10^{-11}$	1.7 (2/120)	8	1.7 (4/234)	10	4.2 (5/120)	24	2.5 (3/120)	10.0	1.6 (3/191)
0.2	4.6 (7/151)	$5.0 \times 10^{-11}$	3.3 (4/124)	10	2.5 (4/155)	15	5.7 (7/123)	32	5.6 (7/125)		
2.0	3.3 (6/182)	$2.12 \times 10^{-10}$	3.7 (7/188)	12	2.1 (2/92)	20	6.2 (12/195)	40	10.3 (14/136)		
20.0	4.1 (12/292)	$5.0 \times 10^{-10}$	3.9 (13/337)	14	2.0 (3/147)	30	7.2 (11/153)				
				16	0.9 (2/224)	40	10.3 (14/136)				

sudden drop in fluid pressure. The mechanism of hydraulically induced fracture is predominately tensile failure, and only very few shear cracks formed when the anisotropic in situ stress is applied (Fig. 4a). As  $\sigma_x \neq \sigma_y$ , the ultimate fracture forms as two major fractures in the horizontal direction which is parallel with the maximum principal stress orientation (Fig. 4b). These results agree well with those predicted by the linear elastic fracture mechanics and observed from previous experimental studies [7, 16, 38], which has been widely applied in the determination of in situ stress orientation.

## 4.2 Effect of operational parameters

The effect of injection fluid viscosity (0.0002, 0.002, 0.02, 0.2, 2.0 and 20 Pa s) is investigated by conducting hydraulic fracturing tests on unconfined samples ( $\sigma_x = \sigma_y = 0$  MPa) with the initial pore pressure  $P_0 = 1.0$  MPa. The injection rate is fixed as  $2.12 \times 10^{-10}$  m<sup>3</sup>/s. As shown in Fig. 5a, the injection pressures for all the cases follow the same trend at the beginning of injection, which increases linearly with time. As relatively high injection rate is adopted, the breakdown pressure can be reached after  $\sim 20$  s when the fluid viscosity is low ( $\mu \leq 0.02$  Pa s). Both the breakdown pressure and the time to fracture follow the similar trend versus the variation of viscosity (Fig. 5b). The breakdown pressure and time to fracture stay constant when  $\mu$  is less than 0.002 Pa s, and increase significantly when  $\mu$  exceeds 0.002 Pa s. Finally, they turn to be constant again once  $\mu$  exceeds 0.2 Pa s. The increase in breakdown pressure with higher viscosity has been observed in the laboratory study [34], and the possible mechanism will be explored in the next section.

As illustrated in Fig. 6, the geometry of fractures changes with the increasing of fluid viscosity. Initially, microcracks are induced around the borehole wall once the tensile stress acting on the bonds exceeds the corresponding strength. When the viscosity is low ( $\mu \leq 0.02$  Pa s), cracks tend to initiate from three sites (point A, point B and point D). After that, fluid flows easily through these cracks and induce more cracks along the initial path. However, two major fractures arise when  $\mu = 0.0002$  Pa s, while three major fractures develop when  $\mu = 0.002$  and 0.02 Pa s. This can be attributed to the fact that increasing of viscosity inhibits the fluid infiltration into fractures along A and D. This leads to the increment of pressure at the tip of crack B and ultimately induces further cracks along B. When  $\mu = 0.2$  Pa s, cracks initiate from four sites and two major fractures develop sub-horizontally follow the path of A and C, respectively. With extremely high viscosity (20 Pa s), five major fractures emerge as fluid is hard to infiltrate into the rock formation and pressure in the

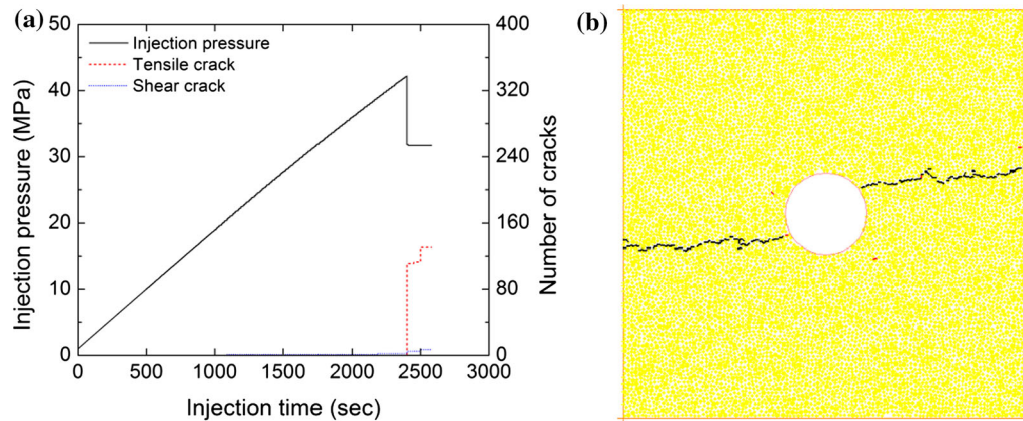


**Fig. 4** **a** Typical case shows the variation of injection pressure and the increment of cracks when the in situ stress state is  $\sigma_x = 15$  MPa,  $\sigma_y = 10$  MPa. **b** Corresponding fracture pattern. The initial pore pressure  $P_0 = 1.0$  MPa. The injection rate equals to  $2.12 \times 10^{-12}$  m<sup>3</sup>/s, and the fluid viscosity equals to 0.2 Pa s. Black short lines represent tensile cracks, and red short lines represent shear cracks (color figure online)

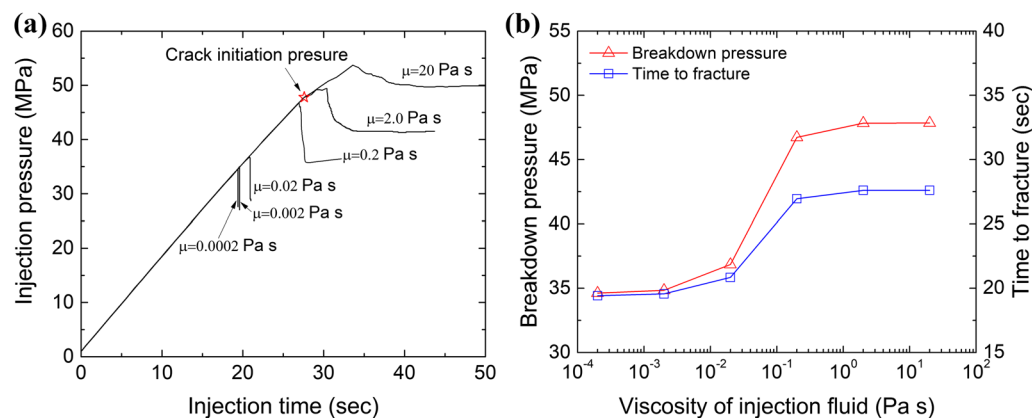


**Fig. 5** Effect of injection fluid viscosity. **a** The increment of injection pressure versus time. **b** Variation of breakdown pressure and time to fracture. The injection rate equals to  $2.12 \times 10^{-10}$  m<sup>3</sup>/s, and the models tested are unconfined samples  $\sigma_x = \sigma_y = 0$  MPa. The initial pore pressure  $P_0 = 1.0$  MPa. Crack initiation pressure is considered in **b** when the viscosity equals to 2.0 and 20 Pa s

hole rises high enough to induce more initial cracks. At the microscale, most of the fractures are formed as tensile cracks, while the shear cracks account for a low proportion (less than 5% as listed in Table 3).

To assess the effect of injection rate, hydraulic fracturing tests with different injection rate ( $2.12 \times 10^{-12}$ ,  $5.0 \times 10^{-12}$ ,  $2.12 \times 10^{-11}$ ,  $5.0 \times 10^{-11}$ ,  $2.12 \times 10^{-10}$  and  $5.0 \times 10^{-10}$  m<sup>3</sup>/s) are performed on unconfined samples with the initial pore pressure  $P_0 = 1.0$  MPa. All the injection pressure curves increase linearly at the initial stage and then drop down sharply after peak. Apparent difference can be noted between the slopes of these curves (Fig. 7a). In general, the lower the injection rate, the longer time it takes to induce fractures. As summarized in Fig. 7b, the breakdown pressure stays constant before the injection rate reaches  $5 \times 10^{-11}$  m<sup>3</sup>/s, while the time to fracture decreases dramatically when the injection rate increases from  $2.12 \times 10^{-12}$  to  $5 \times 10^{-11}$  m<sup>3</sup>/s. Once the injection rate exceeds  $5 \times 10^{-11}$  m<sup>3</sup>/s, the breakdown pressure

increases dramatically with the increase in injection rate, while the time to fracture approaches zero, which means that hydraulic fractures form immediately if the fluid is injected with an extremely high rate. These results are in line with the experimental findings in which the breakdown pressure was found to markedly increase with rate in pressurization rate controlled experiments [38].

Increasing injection rate also alters the geometry of fractures (Fig. 8). Under low injection rate ( $\leq 5.0 \times 10^{-11}$  m<sup>3</sup>/s), cracks initiate from three sites (A, B and D). With the ongoing of tests, two major fractures propagate following the path from point A and point D. These phenomena agree well with the breakdown pressure, which stays constant when the injection rate is lower than  $5.0 \times 10^{-11}$  m<sup>3</sup>/s. Once the injection rate reaches  $2.12 \times 10^{-10}$  m<sup>3</sup>/s, the fluid cannot filtrate into the rock matrix timely, which leads to a higher pressure in the hole and induce one more crack at point C. When the injection rate is further increased to  $5.0 \times 10^{-10}$  m<sup>3</sup>/s, initial cracks

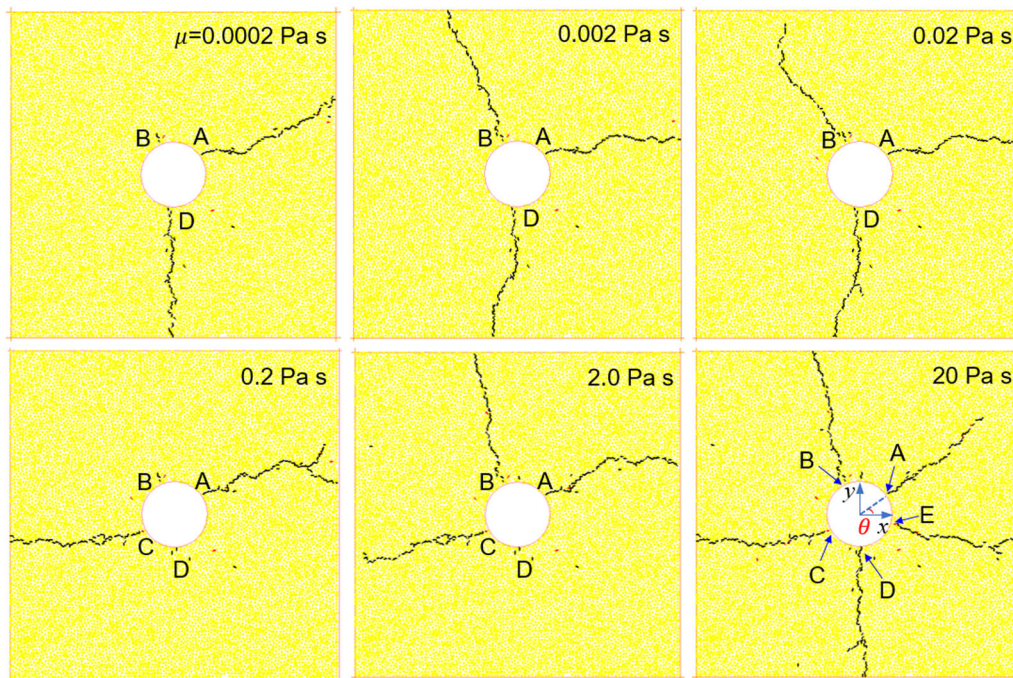


**Fig. 6** Spatial distribution of microcracks at the end of numerical tests conducted on models with different fluid viscosity. Black short lines represent tensile cracks, and red short lines represent shear cracks (color figure online)

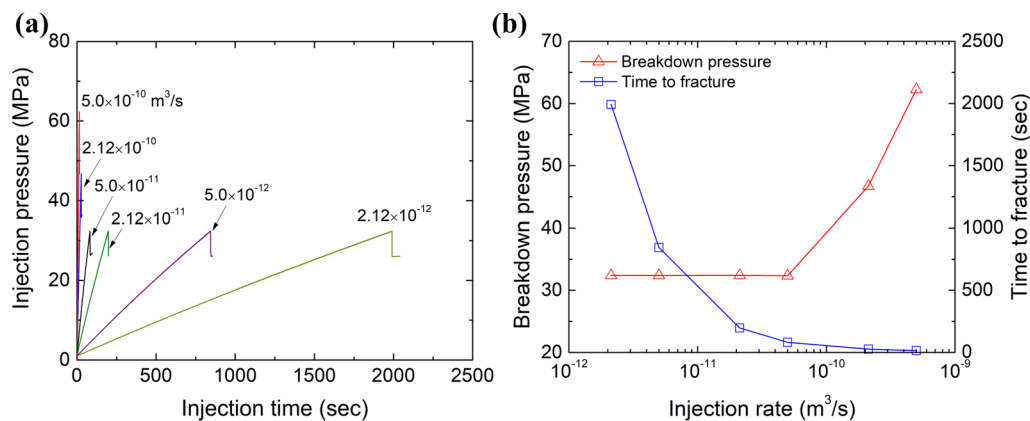


**Fig. 7** Effect of fluid injection rate. **a** The increment of injection pressure versus time. **b** Variation of breakdown pressure and time to fracture. The simulations are conducted on unconfined samples  $\sigma_X = \sigma_Y = 0$  MPa. The viscosity of injection fluid equals to 0.2 Pa s and the initial pore pressure  $P_0 = 1.0$  MPa

can be induced at five sites. Among them, major fractures propagate along A, B, C and E. Bifurcation of fractures can be noted during the propagation of major fracture when the injection rate exceeds  $2.12 \times 10^{-10} \text{ m}^3/\text{s}$  as fluid cannot diffuse rapidly and trigger more than one crack at the tip of fracture. Although the tensile cracks take the majority, percentage of shear cracks increases monotonously with higher injection rate (Table 3).

The effect of borehole diameter ( $D$ ) is examined by conducting hydraulic fracturing tests on unconfined samples with  $D = 4, 6, 8, 10, 12$  and  $14$  mm. The injection rate is fixed as  $2.12 \times 10^{-11} \text{ m}^3/\text{s}$ , and the fluid viscosity

equals to 0.2 Pa s. As illustrated in Fig. 9a, increasing the borehole diameter leads to the decrease in breakdown pressure and the increase in time to failure. It is clearly shown in Fig. 9b that the time to fracture increases almost linearly with the increase in borehole diameter. The breakdown pressure approximately decreases as the diameter increases.

As shown in Fig. 10, orientations of major fractures from models with different borehole diameter are likely random. This can be attributed to the heterogeneity of rock matrix, which leads to the randomly distributed stress and bond strength. Under zero far-field stresses, initiation of



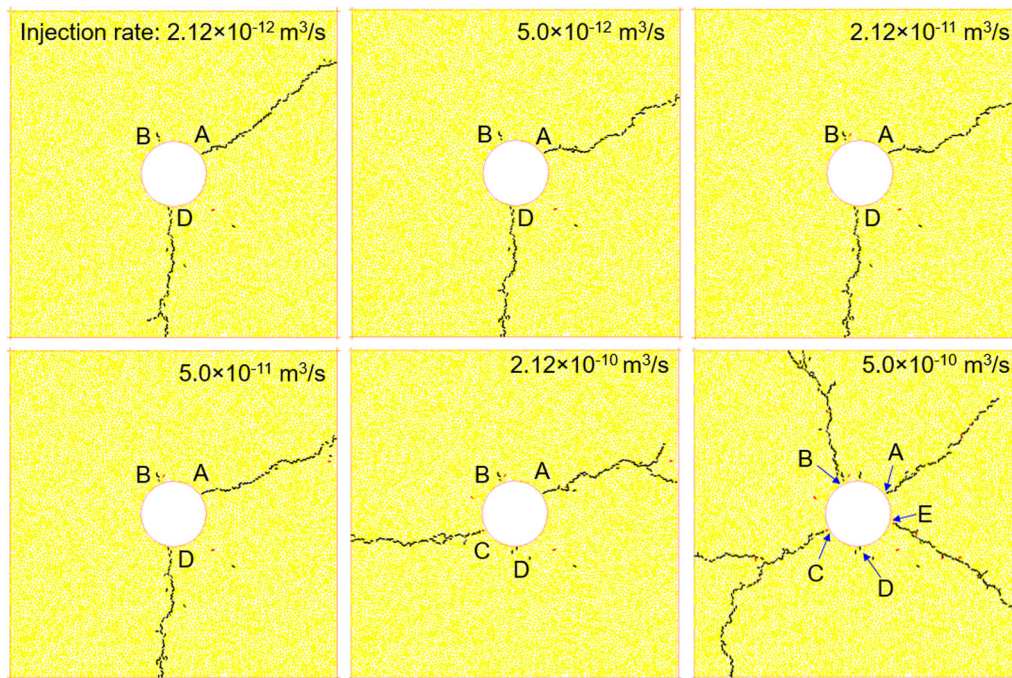


**Fig. 8** Spatial distribution of microcracks at the end of numerical tests conducted on models with different injection rate. Black short lines represent tensile cracks, and red short lines represent shear cracks (color figure online)

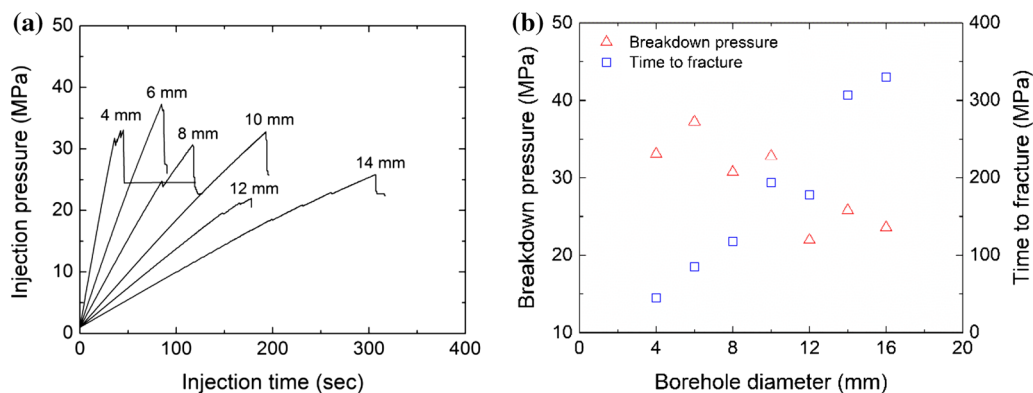


**Fig. 9** Effect of borehole diameter. **a** The increment of injection pressure versus time. **b** Variation of breakdown pressure and the time to fracture. The in situ stress state is  $\sigma_x = \sigma_y = 5$  MPa. The viscosity of injection fluid is 0.2 Pa s, and the injection rate is  $2.12 \times 10^{-11}$  m<sup>3</sup>/s. The initial pore pressure  $P_0 = 1.0$  MPa

cracks is dominated by the stress acting on the bond and the corresponding strength. Thus, models with different borehole diameter may have different sites around the borehole wall with possibility to induce initial cracks. Differences between these sites allow two, three or four major fracture to be developed. For models with different borehole diameter, the percentage of shear cracks stays almost constant at a low level (less than 3%).

### 4.3 Effect of in situ states

Two scenarios are designed to explore the influences of the in situ stress states. The first scenario, which is discussed in

this paragraph, monotonously raises the confining pressure from 5 MPa to 40 MPa by keeping  $\sigma_x = \sigma_y$ . The second scenario, which is discussed in the next paragraph, investigates the influence of in situ stress anisotropy with  $\sigma_y$  fixed as 40 MPa, and  $\sigma_x$  varies. As can be observed in Fig. 11a, the injection pressure follows the same trend at the beginning of injection, which increases linearly until the occurrence of fractures. The breakdown pressure increases from  $\sim 30$  MPa to more than 70 MPa as the in situ stress varies from 5 to 40 MPa (Fig. 8b). The fracture initiation pressure refers to the pressure at which the fractures start to occur. The crack initiation pressure deviates from the breakdown pressure when the in situ

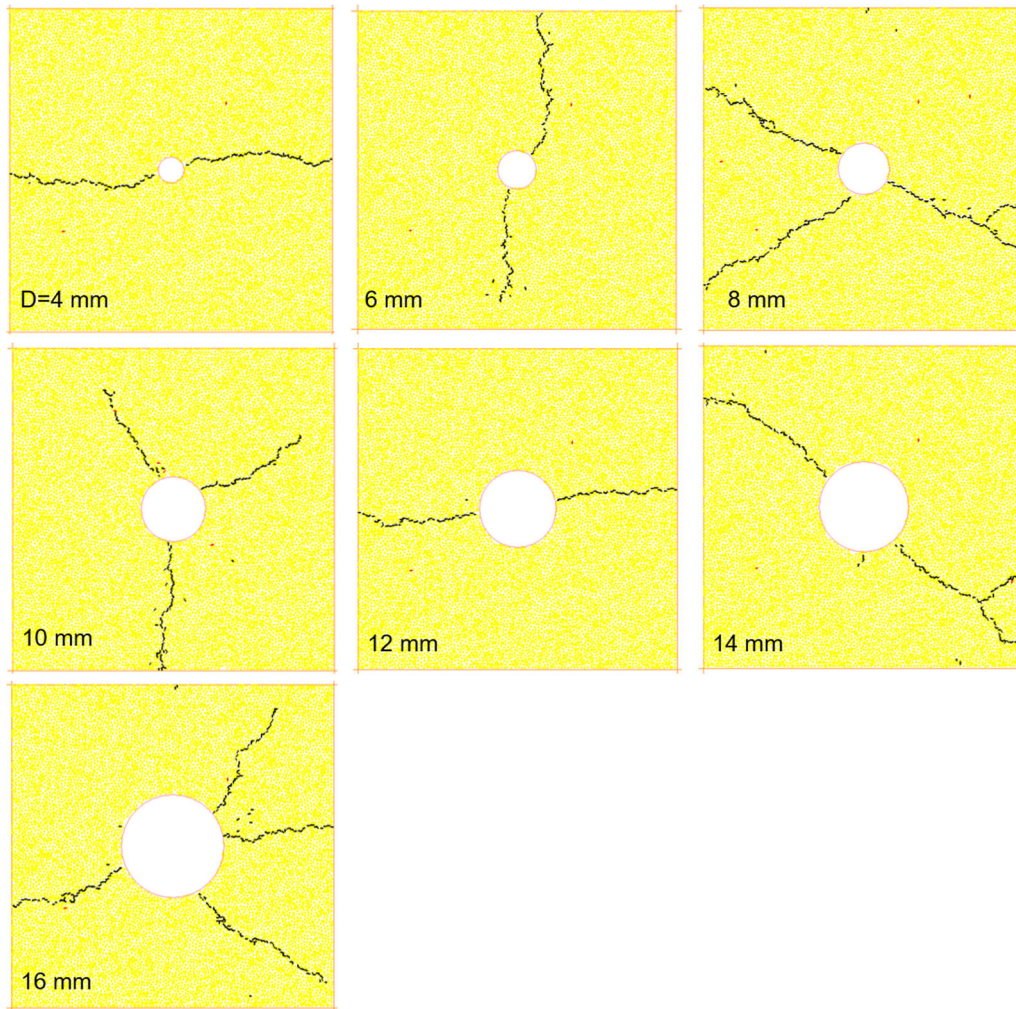


**Fig. 10** Spatial distribution of microcracks at the end of numerical tests conducted on models with different borehole diameter. Black short lines represent tensile cracks, and red short lines represent shear cracks (color figure online)

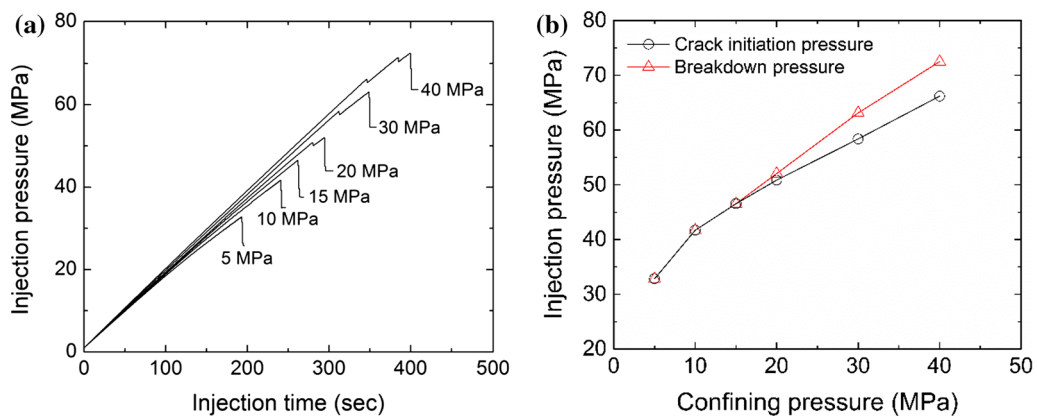


**Fig. 11** Effect of in situ stress state ( $\sigma_x = \sigma_y$ ). **a** The increment of injection pressure versus time. **b** Variation of crack initiation pressure and breakdown pressure. The injection rate is  $2.12 \times 10^{-11} \text{ m}^3/\text{s}$ , the viscosity of injection fluid equals to  $0.2 \text{ Pa s}$ , and the initial pore pressure  $P_0 = 1.0 \text{ MPa}$

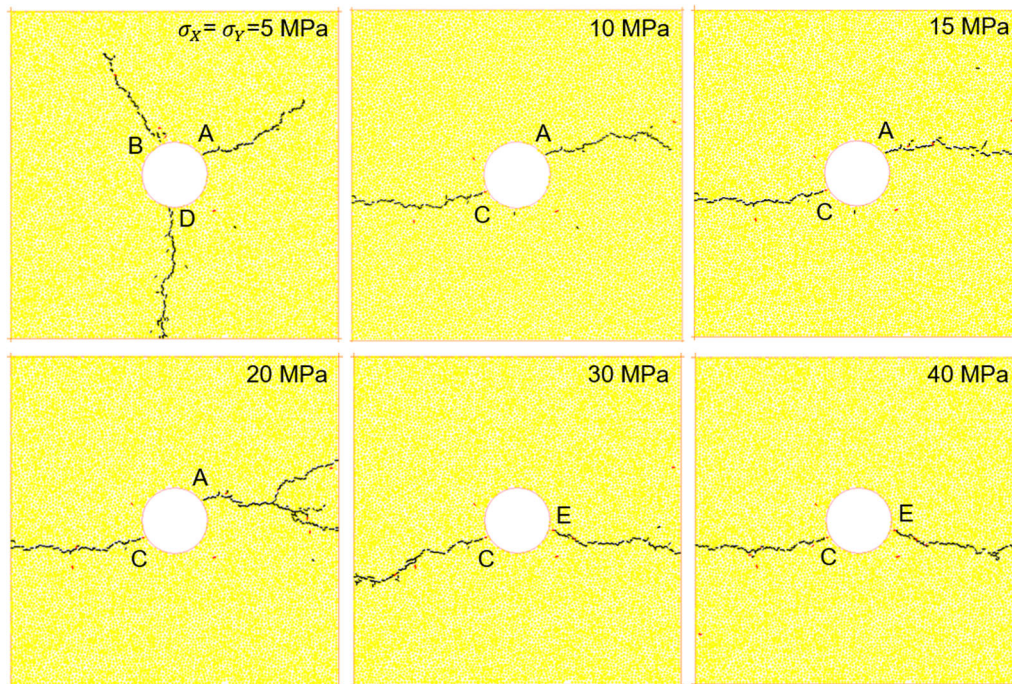


**Fig. 12** Spatial distribution of microcracks at the end of numerical tests conducted on models with different in situ stress by keeping  $\sigma_X = \sigma_Y$ . Black short lines represent tensile cracks, and red short lines represent shear cracks (color figure online)

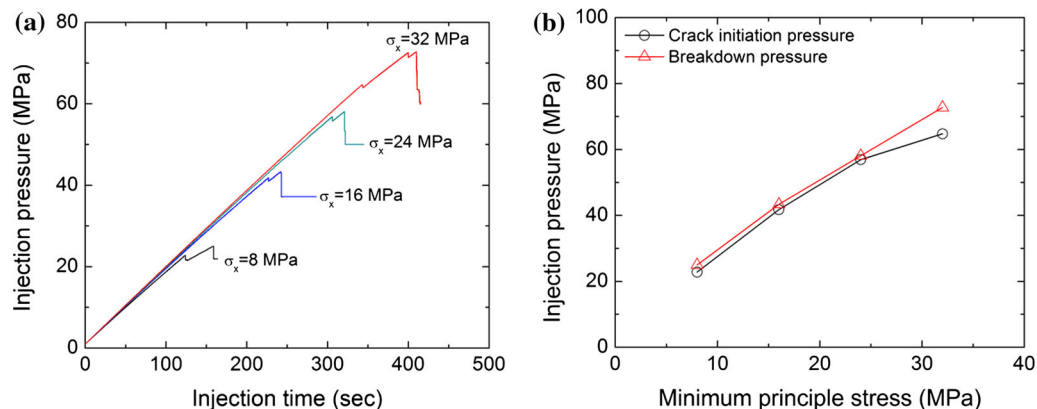


**Fig. 13** Effect of the minimum principle stress ( $\sigma_X$ ). **a** The increment of injection pressure versus time. **b** Variation of the crack initiation pressure and the breakdown pressure. The maximum principle stress is fixed as  $\sigma_Y = 40$  MPa for all the cases. The initial pore pressure is 1 MPa. The fluid injection rate equals to  $2.12 \times 10^{-11}$  m<sup>3</sup>/s, and the injection fluid viscosity equals to 0.2 Pa s

stress reaches 20 MPa, and the difference between the breakdown pressure and the initiation pressure increases monotonously with the increase in confining pressure (Fig. 11b).

Under hydrostatic in situ stresses, the orientation of major fractures varies with the stress magnitude (Fig. 12). Although all the fractures initiate from point A and point C when  $\sigma_X = \sigma_Y \geq 10$  MPa, they follow various path with the ongoing of tests. Under different in situ stress states, heterogeneity of local stress may alter the permeability of each pipes, which in turn results in the difference between pore pressures. Thus, fractures may propagate along

different paths. The percentage of shear cracks increases almost linearly with the increasing of in situ stress (Table 3), which implies that the role of shear cracks becomes more significant with the high in situ stress level.

The effect of in situ stress anisotropy evaluated by maintaining  $\sigma_Y = 40$  MPa and gradually reducing  $\sigma_X$  to 32, 24, 16 and 8 MPa, respectively. As illustrated in Fig. 13a, the injection pressure also follows the same trend at the initial stage. The breakdown pressure increases linearly versus the minimum principal stress. The difference between crack initiation pressure and breakdown pressure exists in all these cases (Fig. 13b). This difference stays

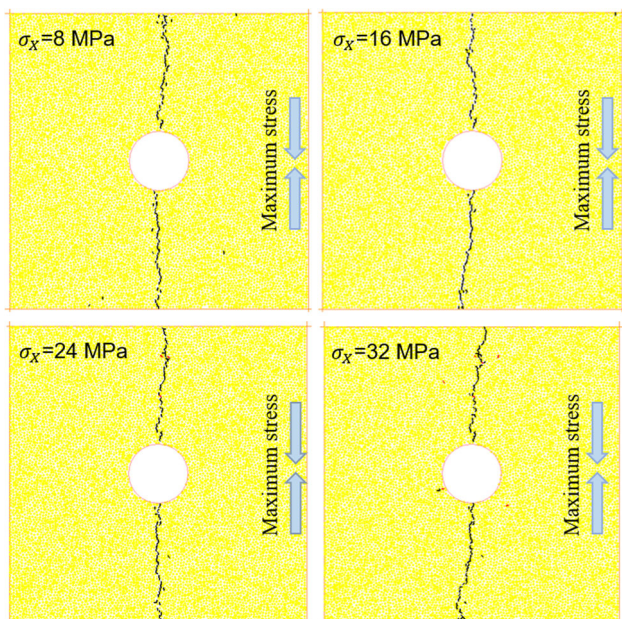


**Fig. 14** Spatial distribution of microcracks at the end of numerical tests conducted on models with different minimum stress ( $\sigma_Y$ ), while the maximum principal stress ( $\sigma_X$ ) is fixed as 40 MPa. Black short lines represent tensile cracks, and red short lines represent shear cracks (color figure online)

almost constant when  $\sigma_X \leq 24$  MPa, but increases to a high value once  $\sigma_X$  reaches to 32 MPa.

When the in situ stresses are unequal, major fractures always propagate along the orientation of maximum principal stress (vertical direction in Fig. 14). However, differences exist between the mechanisms of microcracks. As compared in Table 3, the percentage of shear cracks increases from 0.0% to more than 10% when the minimum principal stress rises from 8 MPa to hydrostatic state (40 MPa). Therefore, shear failure is easy to form under equivalent in situ stress.

The influence of initial pore pressure ( $P_0$ ) is assessed by conducting injection tests with constant rate ( $2.12 \times 10^{-11}$

$\text{m}^3/\text{s}$ ) on saturated samples with  $P_0 = 1, 5$  and 10 MPa. The in situ stress state is  $\sigma_X = \sigma_Y = 5$  MPa. It can be observed from Fig. 15a that the injection pressure curves are almost parallel with each other. These curves increase linearly with time till the breakdown pressure is reached, followed by a sharp drop. As presented in Fig. 15b, increasing initial pore pressure results in the reduction in breakdown pressure as well as the decrease in the time to fracture.

As shown in Fig. 16, change of initial pore pressure does not influence the sites at which initial cracks can be induced. Major fractures starting from D follow the same vertical path for all the cases. Obvious change can be noted from the orientation of fractures develop from A and B. The percentage of shear cracks stays almost constant with the change of pore pressure. Thus, the initial pore pressure plays a less significant role on the geometry and mechanism of fractures.

### 5 Discussions

During the fluid injection, fracturing occurs when the tangential effective stress reaches the tensile resistance at a critical location around the borehole wall. When the formation is impermeable, no poroelastic effect exists and the breakdown pressure ( $P_b$ ) can be obtained from Eq. 4.b [12, 20]:

$$P_b = T + 3\sigma_h - \sigma_H - P_0 \tag{6}$$

where  $T$  denotes the tensile resistance of the rock formation.

When the rock matrix is permeable, the pressurized fluid may penetrate into the surrounding rock prior to fracturing and thus perturb the stress field by increasing the interstitial pore pressure around the borehole [38]. The effect of fluid infiltration into the borehole wall and its corresponding

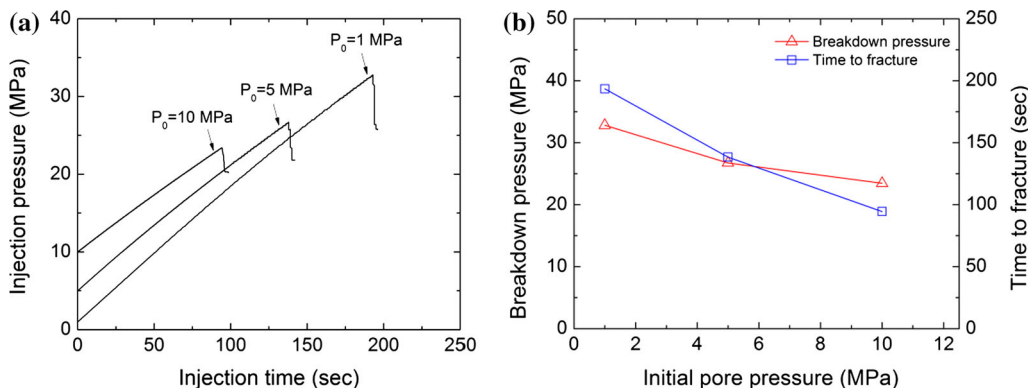


**Fig. 15** Effect of initial pore pressure. **a** The increment of injection pressure versus time. **b** Variation of the breakdown pressure and the time to fracture. The in situ stress state is  $\sigma_X = \sigma_Y = 5$  MPa. The viscosity equals to 0.2 Pa s, and the injection rate is  $2.12 \times 10^{-11} \text{ m}^3/\text{s}$ . The initial pore pressure is 1, 5 and 10 MPa, respectively

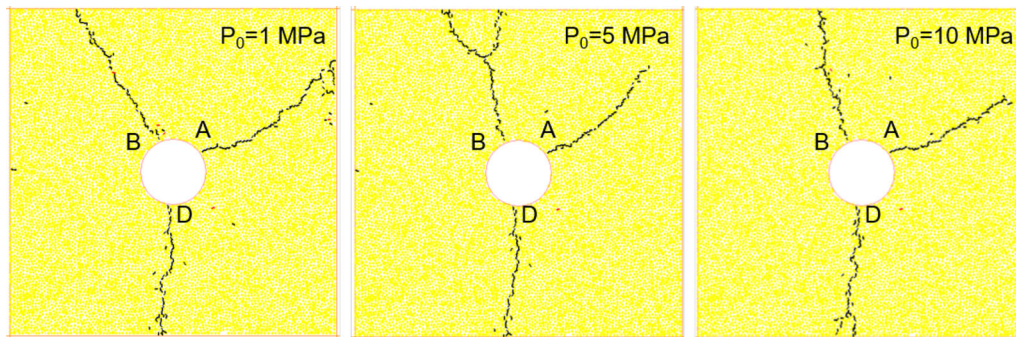


**Fig. 16** Spatial distribution of microcracks at the end of numerical tests conducted on models with different initial pore pressure ( $P_0$ ). Black short lines represent tensile cracks, and red short lines represent shear cracks (color figure online)

influence on breakdown pressure magnitude can be described by the Biot effective stress theory [12, 15]. Based on the Haimson–Fairhurst (H–F) solution [17] and the effective stress theory, the breakdown pressure can be calculated as:

$$P_b = \frac{3\sigma_h - \sigma_H - P_0 + T}{1 + \eta} \quad (7)$$

where  $\eta = \frac{\nu}{1-\nu}\alpha$ .  $\nu$  is the Poisson's ratio, and  $\alpha$  is the Biot coefficient [12].

The breakdown pressures for boreholes in impermeable and permeable media can be calculated from Eqs. 6 and 7, respectively. The theoretical solutions suggest that the breakdown pressure should be a function of the ambient stress ( $\sigma_h$ ,  $\sigma_H$  and  $P_0$ ) and the tensile resistance of the rock ( $T$ ). As discussed in Sect. 4,  $P_b$  increases linearly with  $\sigma_H$  when  $\sigma_H = \sigma_h$  (Fig. 11b). When  $\sigma_H$  is fixed,  $P_b$  increases linearly with  $\sigma_h$  (Fig. 13b).  $P_b$  decreases linearly with  $P_0$  when both  $\sigma_H$  and  $\sigma_h$  are fixed (Fig. 15b). These results confirm that the influences of the in situ stresses ( $\sigma_H$  and  $\sigma_h$ ) and the initial pore pressure ( $P_0$ ) can be captured by the DEM model. However, the theoretical solutions do not consider the breakdown pressure as a function of injection rate and viscosity, which has been revealed in previous experimental studies [3, 12, 34, 38] and confirmed by the simulation results of this study.

The greater pressure required to fracture the model when a high-viscosity fluid or high injection rate is adopted is likely the result of the size effect on tensile resistance of the formation as will be discussed in the following section. Figure 17a compares the contact force network from models close to the breakdown pressure when the injection rate is  $2.12 \times 10^{-10} \text{ m}^3/\text{s}$  and  $\mu = 2.0$  and  $0.002 \text{ Pa s}$ , respectively. It is apparent that strong forces concentrate around the borehole wall when the viscosity is high. The dissipation of contact force becomes more moderate when the viscosity is low as the model with lower viscosity is easier to be infiltrated. A series of measurement circles are installed along the  $x$ -axis with the diameter of 2 mm, and

the distance between nearby circles equals to 1 mm. Stress components calculated from Eq. 5 are normalized by the breakdown pressure for the ease of comparison. As illustrated in Fig. 17b, the range of model under tension (in the tangential direction) is  $x = 8.9 \text{ mm}$  when  $\mu = 2.0 \text{ Pa s}$ , whereas this range increases to  $x = 16.6 \text{ mm}$  when  $\mu = 0.002 \text{ Pa s}$ .

Similar responses can be observed from the cases with  $\mu = 2.0 \text{ Pa s}$ , and the injection rate equals to  $2.12 \times 10^{-10}$  and  $2.12 \times 10^{-12} \text{ m}^3/\text{s}$ , respectively (Fig. 17c, d). With the injection rate increases from  $2.12 \times 10^{-12}$  to  $2.12 \times 10^{-10} \text{ m}^3/\text{s}$ , the range of model under tension in the tangential direction raises from 8.2 to 22.6 mm (shown by the range filled in Fig. 17d with blue and red, respectively). Therefore, when a low-viscosity fluid or a low injection rate is used, the fluid infiltrates into the medium easily and the affected area is large (indicated in Fig. 17e).

Tensile strengths measured from direct tensile tests conducted on DEM model with different scales (with the length to width ratio  $L/W$  fixed as 2.0) are compared in Fig. 17f. It is apparent that the tensile strength increases with the reduction in sample size. Therefore, the less fluid penetrates through the medium, the higher apparent tensile strength appears, which is in line with the conceptual model proposed to explain anomalously high breakdown pressure obtained with high-viscosity fluid [38]. When the viscosity is extremely high, the fluid is hard to infiltrate the medium, and injection-induced bond breakage tends to occur only in the first layer of particles next to the borehole wall. The corresponding tensile strength approaches to the strength of a single bond which equals to  $60 \pm 13.5 \text{ MPa}$  (see Table 1). That is why the breakdown pressure in Fig. 5b approaches to a stable magnitude of  $\sim 47 \text{ MPa}$ , which is consistent with the minimum bond strength. In Fig. 5b, the breakdown pressure stays almost constant when  $\mu \leq 0.002 \text{ Pa s}$  as the tensile strength tends to be constant with the increase in sample size.

The reduction in breakdown pressure with the increase in borehole diameter can also be attributed to the fact that

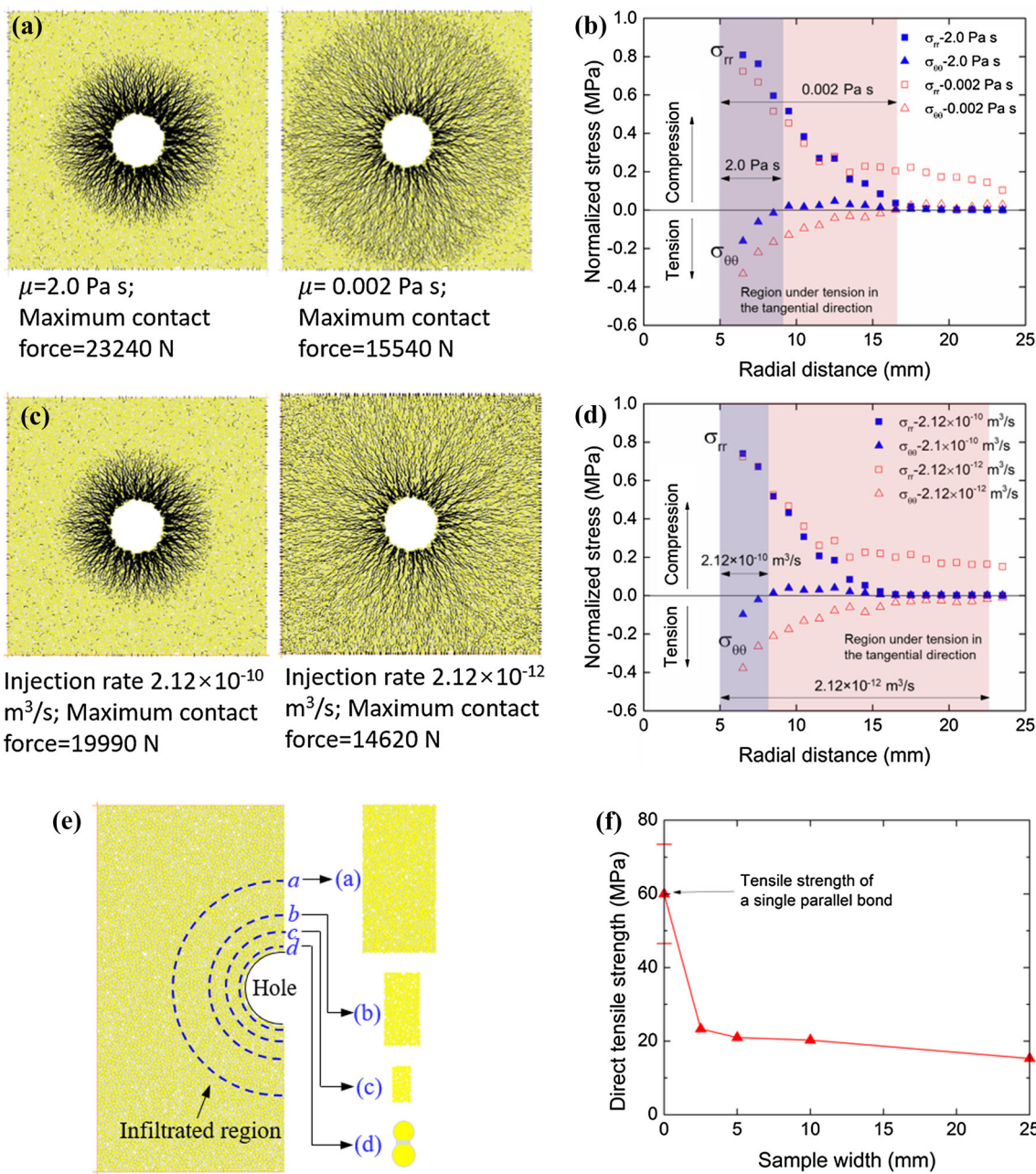


**Fig. 17** **a** Contact force network from unconfined models around the peak injection pressure when the injection rate equals to  $2.12 \times 10^{-10} \text{ m}^3/\text{s}$  and  $\mu = 2.0$  and  $0.002 \text{ Pa s}$ , respectively; **b** variation of stresses along the  $x$ -axis. The stress components are normalized by the breakdown pressure. Regions under tension in the tangential direction are filled with blue when  $\mu = 2.0 \text{ Pa s}$  and red when  $\mu = 0.002 \text{ Pa s}$ ; **c** contact force network from unconfined models around the peak injection pressure when  $\mu = 0.2 \text{ Pa s}$  and the injection rate equals to  $2.12 \times 10^{-10}$  and  $2.12 \times 10^{-12} \text{ m}^3/\text{s}$ , respectively; **d** variation of stresses along the  $x$ -axis. The stress components are normalized by the breakdown pressure. Regions under tension in the tangential direction are filled with blue when the rate equals to  $2.12 \times 10^{-10} \text{ m}^3/\text{s}$  and red when the rate is  $2.12 \times 10^{-12} \text{ m}^3/\text{s}$ ; **e** diagram illustrates the effect of fluid infiltration range on the tensile strength of rock sample. The infiltrated regions are defined by the dashed lines. The corresponding samples under tensile stress are shown in the right column. **f** Variation of direct tensile strength versus the sample width measured from samples with the ratio length/width fixed as 2.0. Strength of a single parallel bond is represented as  $W = 0$  (color figure online)

the interaction area becomes larger with the increase in borehole size which ultimately leads to the reduction in tensile strength. This type of size effect also exists in the realistic rock formation, as the increase in sample scale

results in the existence of more pores, weak layers, and fissures which ultimately reduce the tensile strength of rock blocks. The practical implications of these results lie in the adoption of fracturing fluid with low viscosity, e.g., the

critical state CO<sub>2</sub> [34]. In addition, appropriate injection rate which optimizes the breakdown pressure and the time needed to induce fractures should be estimated.

It is worth pointing out that all simulation results discussed in this study are obtained from DEM samples with constant particle size/size distribution. Although we have observed the same trend of borehole size effect in the numerical model as in the laboratory, the magnitude of borehole size effect observed is not the same as in reality unless the model particle size matches the grain size, which is still difficult at current stage due to the limitation of computational capacity. We intend to qualitatively explore the effect of borehole diameter through a suite of comparative studies. Although the fracture toughness of DEM model is proved to be dependent on the selection of particle size [26], both the breakdown pressure and the direct tensile strength measured in our manuscript are conducted on models with the same particle size/size distribution. In Fig. 17, we normalize the stress around the borehole wall by the breakdown pressure. Nevertheless, it is advised that direct application of the modeling results to interpret physical problems is not appropriate. Further studies are necessary to elucidate the influence of particle size chosen in the DEM model on the hydraulic fracturing responses.

## 6 Conclusions

Fully coupled DEM model is constructed to simulate the hydraulic fracturing in permeable rock formation at laboratory scale. The validity of the model is examined by comparing the stress distribution around the borehole wall with analytical solutions, between which good agreements can be found.

Systematic parametric studies are then performed to evaluate the influence of operational parameters (e.g., viscosity, injection rate and borehole diameter) and in situ conditions (e.g., in situ stress state and initial pore pressure). The operational parameters play a major role as the breakdown pressure increases significantly with the increase in viscosity when its magnitude is between 0.002 and 0.2 Pa s. Increasing the injection rate substantially shortens the time to fracture but increases the breakdown pressure when it exceeds  $5 \times 10^{-11}$  m<sup>3</sup>/s in this study. Simulation results also reveal that the breakdown pressure increases linearly with the in situ stress magnitude and decreases linearly with the initial pore pressure.

Comparison between the poroelasticity theory and modeling results confirms that the variation of breakdown pressure with viscosity, injection rate and borehole diameter can be attributed to the size effect of tensile strength with different infiltrated regions. Under unequal in situ stresses, major fractures always propagate along the

orientation of maximum principal stress. Under hydrostatic stress state, the geometry of major fractures might be affected by the injection rate, viscosity and stress magnitude. Tensile cracks dominate the hydraulic fractures, while the percentage of shear cracks monotonically increases with in situ stress under hydrostatic stress state. Micromechanical analyses performed in this study sheds light on the cause of high breakdown pressure with high viscosity and injection rate. Further study is necessary to build guidelines for the selection of operational parameters when one conducts hydraulic fracturing in rock formation under various in situ conditions.

**Acknowledgements** The authors would like to appreciate the two anonymous reviewers for their constructive comments.

## References

- Adachi J, Siebrits E, Peirce A, Desroches J (2007) Computer simulation of hydraulic fractures. *Int J Rock Mech Min* 44:739–757
- Al-Busaidi A, Hazzard J, Young R (2005) Distinct element modeling of hydraulically fractured Lac du Bonnet granite. *J Geophys Res Solid Earth* 1978–2012:110
- Bohlooli B, de Pater CJ (2006) Experimental study on hydraulic fracturing of soft rocks: influence of fluid rheology and confining stress. *J Petrol Sci Eng* 53:1–12
- Bonilla-Sierra V, Scholtès L, Donzé FV, Elmouttie MK (2015) Rock slope stability analysis using photogrammetric data and DFN–DEM modelling. *Acta Geotech* 10:497–511
- Cundall PA, Strack OD (1979) A discrete numerical model for granular assemblies. *Geotechnique* 29:47–65
- Damjanac B, Detournay C, Cundall PA (2016) Application of particle and lattice codes to simulation of hydraulic fracturing. *Comput Part Mech* 3:249–261
- Detournay E (2016) Mechanics of hydraulic fractures. *Annu Rev Fluid Mech* 48:311–339
- Duan K, Kwok C (2016) Evolution of stress-induced borehole breakout in inherently anisotropic rock: insights from discrete element modeling. *J Geophys Res Solid Earth* 121:2361–2381
- Duan K, Kwok CY, Ma X (2017) DEM simulations of sandstone under true triaxial compressive tests. *Acta Geotech* 12:495–510
- Duan K, Kwok CY, Pierce M (2016) Discrete element method modeling of inherently anisotropic rocks under uniaxial compression loading. *Int J Numer Anal Meth Geomech* 40:1150–1183
- Fatahi H, Hossain MM, Fallahzadeh SH, Mostofi M (2016) Numerical simulation for the determination of hydraulic fracture initiation and breakdown pressure using distinct element method. *J Nat Gas Sci Eng* 33:1219–1232
- Gan Q, Elsworth D, Alpern JS, Marone C, Connolly P (2015) Breakdown pressures due to infiltration and exclusion in finite length boreholes. *J Petrol Sci Eng* 127:329–337
- Goodfellow SD, Nasser MHB, Maxwell SC, Young RP (2015) Hydraulic fracture energy budget: insights from the laboratory. *Geophys Res Lett* 42:3179–3187
- Grassl P, Fahy C, Gallipoli D, Wheeler SJ (2015) On a 2D hydro-mechanical lattice approach for modelling hydraulic fracture. *J Mech Phys Solids* 75:104–118

15. Haimson B (1968) Hydraulic fracturing in porous and nonporous rock and its potential for determining in situ stresses at great depth. Minnesota University, Minneapolis
16. Haimson B (2007) Micromechanisms of borehole instability leading to breakouts in rocks. *Int J Rock Mech Min* 44:157–173
17. Haimson B, Fairhurst C (1967) Initiation and extension of hydraulic fractures in rocks. *Soc Petrol Eng J* 7:310–318
18. Haimson BC, Zhao Z (1991) Effect of borehole size and pressurization rate on hydraulic fracturing breakdown pressure. In: The 32nd US symposium on rock mechanics (USRMS). American Rock Mechanics Association
19. Hazzard JF, Young RP, Maxwell SC (2000) Micromechanical modeling of cracking and failure in brittle rocks. *J Geophys Res Solid Earth* 105:16683–16697
20. Hubbert MK, Willis DG (1957) Mechanics of hydraulic fracturing. *US Geol Surv* 210:153–168
21. Itasca (2008) PFC2D particle flow code in 2 dimensions, 4.0th edn. Itasca, Minneapolis
22. Labra C, Rojek J, Oñate E, Zarate F (2008) Advances in discrete element modelling of underground excavations. *Acta Geotech* 3:317–322
23. Li L, Meng Q, Wang S, Li G, Tang C (2013) A numerical investigation of the hydraulic fracturing behaviour of conglomerate in Glutenite formation. *Acta Geotech* 8:597–618
24. Newman Jr J (1971) An improved method of collocation for the stress analysis of cracked plates with various shaped boundaries. NASA Tech. Note D-6373. Langley Research Center, Hampton
25. Potyondy DO (2015) The bonded-particle model as a tool for rock mechanics research and application: current trends and future directions. *Geosyst Eng* 18:1–28
26. Potyondy DO, Cundall PA (2004) A bonded-particle model for rock. *Int J Rock Mech Min* 41:1329–1364
27. Pruess K (2006) Enhanced geothermal systems (EGS) using CO<sub>2</sub> as working fluid—a novel approach for generating renewable energy with simultaneous sequestration of carbon. *Geothermics* 35:351–367
28. Shimizu H, Murata S, Ishida T (2011) The distinct element analysis for hydraulic fracturing in hard rock considering fluid viscosity and particle size distribution. *Int J Rock Mech Min* 48:712–727
29. Tomac I, Gutierrez M (2015) Formulation and implementation of coupled forced heat convection and heat conduction in DEM. *Acta Geotech* 10:421–433
30. Tomac I, Gutierrez M (2017) Coupled hydro-thermo-mechanical modeling of hydraulic fracturing in quasi-brittle rocks using BPM-DEM. *J Rock Mech Geotech Eng* 9:92–104
31. Warpinski NR, Mayerhofer MJ, Vincent MC, Cipolla CL, Lolon E (2009) Stimulating unconventional reservoirs: maximizing network growth while optimizing fracture conductivity. *J Can Pet Technol* 48:39–51
32. Wu W, Zoback MD, Kohli AH (2017) The impacts of effective stress and CO<sub>2</sub> sorption on the matrix permeability of shale reservoir rocks. *Fuel* 203:179–186
33. Zhang X, Jeffrey RG, Thiercelin M (2009) Mechanics of fluid-driven fracture growth in naturally fractured reservoirs with simple network geometries. *J Geophys Res Solid Earth* 114:B12406
34. Zhang X, Lu Y, Tang J, Zhou Z, Liao Y (2017) Experimental study on fracture initiation and propagation in shale using supercritical carbon dioxide fracturing. *Fuel* 190:370–378
35. Zhao X, Young P (2011) Numerical modeling of seismicity induced by fluid injection in naturally fractured reservoirs. *Geophysics* 76:WC167–WC180
36. Zhou J, Jin Y, Chen M (2010) Experimental investigation of hydraulic fracturing in random naturally fractured blocks. *Int J Rock Mech Min* 47:1193–1199
37. Zoback MD, Moos D, Mastin L, Anderson RN (1985) Well bore breakouts and in situ stress. *J Geophys Res Solid Earth* 1978–2012(90):5523–5530
38. Zoback MD, Rummel F, Jung R, Raleigh CB (1977) Laboratory hydraulic fracturing experiments in intact and pre-fractured rock. *Int J Rock Mech Min Sci Geomech Abstr* 14:49–58